Influence of the Lamination Material and Rotor Pole Geometry on the Performance of Wound Field Synchronous Machines

Influence of the Lamination Material and Rotor Pole Geometry on the Performance of Wound Field Synchronous Machines

Marco Biasion
Student Member, IEEE
Politecnico di Torino
Dipartimento Energia
Torino, Italy
marco.biasion@polito.it

Damian Kowal
ABB Corporate Research
Västerås, Sweden
damian.kowal@se.abb.com

Reza Rajabi Moghaddam
Researcher
Västerås, Sweden
Rrajabi2001@yahoo.com

Michele Pastorelli
Member, IEEE
Politecnico di Torino
Dipartimento Energia
Torino, Italy
michele.pastorelli@polito.it

***Abstract*— This paper examines the influence of the lamination material and rotor pole geometry on the steady-state performance of a wound field synchronous machine operated in the generating mode. The investigations are carried out through 2D finite element analyses using a commercial software package. Non-Oriented silicon-iron alloys of various grades are selected to recognize the impact of their magnetic properties on the machine performance. Different methods for the extrapolation of *BH* curves from low-medium field levels to saturation are reviewed and compared.**
The effect of using different materials on both the rotor and the stator core is assessed in terms of variation of the air gap power, the torque ripple and the core losses. The performance of a new machine featuring a higher-grade lamination material and a refined rotor pole geometry are compared at constant air gap power with those of the reference machine.
The results show that, depending on the adopted strategy, it is possible to almost halve the torque ripple and slightly decrease the mass of the rotor core.

Keywords*— *Electrical machines, wound field synchronous machines, magnetic materials, electrical steel sheets, silicon-iron, core losses, refinement of machine dimensions, machine design.

I. Introduction

Wound Field Synchronous Machines (WFSMs) have been employed as power generators since the late 19th century and their use in electric vehicle applications has also received much interest in recent times. WFSMs do not require the use of rare-earth permanent magnet materials, exhibit good flux weakening capabilities and allow to improve the system efficiency [1], [2].

The electromagnetic sizing of electrical machines is usually carried out with analytical equations first, then the obtained layout is usually refined and optimized through numerical analyses. Nonlinear simulations based on the finite-element method (FEM) currently represent a consolidated solution for the computer-aided design of electrical machines. Common numerical investigations on the machine normally include studies of its behavior in various operating conditions, and evaluations of the impact of different materials and/or refinements of the initial geometry.

The impact of the core material grade on the performance of induction motors, permanent-magnet synchronous generators and synchronous reluctance motors was already assessed in different studies [3]–[5]. The results showed that the use of a different material grade for the core can affect the efficiency, the average torque, and the torque ripple of the machine [3], [5]. Insights on how to optimize the machine geometry can be also obtained from such investigations [4].

Different strategies for optimizing and refining the rotor geometry of WFSMs have been proposed in the literature so far. The modification of the rotor pole surface, considering both symmetrical and asymmetrical geometries, and the use of slits or barriers were investigated in [6]–[8]. The studies were mainly focused on decreasing the torque ripple, reducing the core losses and improving the saliency of the machine.

Accurate investigations on the influence of different core materials and core geometries on the machine performance require a meticulous characterization and modeling of the materials for electrical machines. Soft magnetic materials can be characterized complying with standard methodologies, such as the Epstein frame method [9]. However, their behavior at high field levels and in saturated conditions is seldom evaluated in practice. This may represent an issue, especially when carrying out numerical analyses of electrical machines that present local saturation of the magnetic core. The study reported in [10] highlighted that the incorrect extrapolation to saturation of the measured *BH* curves may lead to substantial simulation errors.

The analysis of the points mentioned above leads to two conclusions. First, the evaluation of the impact of both the material grade and the rotor geometry on the performance of WFSMs must be improved. Second, awareness must be raised within the research community on the importance of the accurate modeling of material properties in numerical simulations.

This paper explores the influence of different lamination materials and rotor pole geometries on the steady-state performance of a 1.16 MW, three-phase, four-pole, 50 Hz WFSM operated in the generating mode. The machine is analyzed in rated conditions by means of 2D time-stepping FEM simulations. The analysis of several non-oriented (NO) silicon-iron (SiFe) alloys highlights the capital importance of a proper modeling of their *BH* curves at medium-high field levels in numerical simulations. The influence of different rotor and stator lamination materials on the machine performance is investigated afterwards. The impact of a different rotor pole geometry on the performance is assessed by changing the *d*-axis air gap size, the dimensions of the rotor pole neck and the design of the rotor pole shoe. The results show that, depending on the adopted strategy, the modification of the rotor pole geometry and the use of a high-grade lamination material can contribute to substantially reduce the torque ripple and slightly decrease the rotor mass. This at the expense of an increase of the core losses.

This research work was supported by ABB Corporate Research Center, Västerås, Sweden.

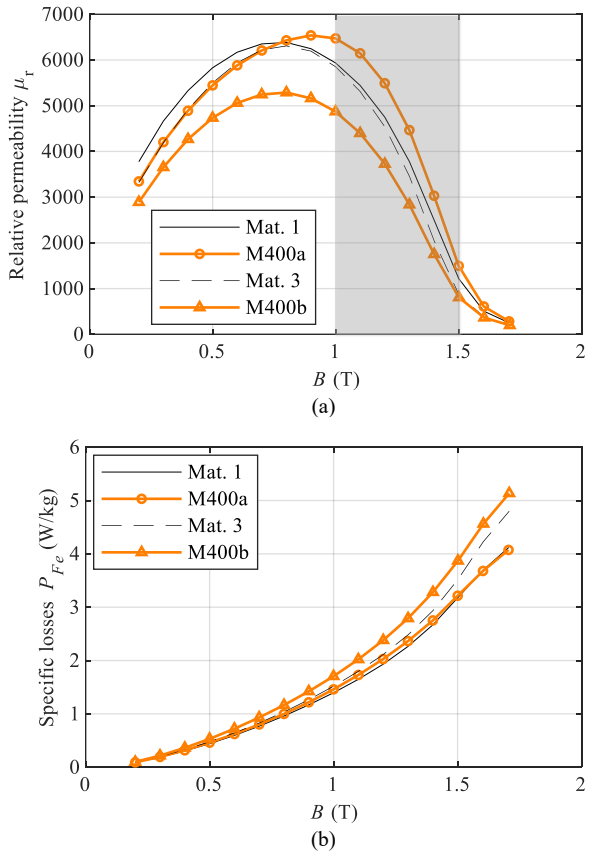

Fig. 1. The magnetic properties of four samples of the M400-50A material grade. (a) Relative permeability vs. magnetic flux density and (b) the specific power losses vs. magnetic flux density. The materials with the highest and the lowest relative permeability in the range 1-1.5 T were selected (M400a and M400b).

II. Selection of the Lamination Materials for the Core

The laminated iron core of electrical machines is typically manufactured using electrical steel sheets with thicknesses of 0.2÷1 mm. This work focuses on NO SiFe laminated steels, and the investigated grades are M270-50A, M330-35A, M400-50A, M700-50A and M600-65A; they were provided by different manufacturers. The materials were characterized experimentally in the form of strips using a commercial Epstein frame tester, and performing the measurements following the IEC 60404-2 standard under sinusoidal flux density excitation [9].

The properties of the strips from different manufacturers were compared for each grade; due to the relevant number of available samples, only some of them were selected for the investigations in the machine. The following illustrates the selection process for the strips belonging to the grade M400-50A, but all the other grades were treated in the same manner.

The strips were selected evaluating the value of the relative permeability μ_r; the chosen ones were those exhibiting the highest and the lowest value for μ_r in the range of the magnetic flux density B = 1-1.5 T. The choice of this range for the flux density is related to its common values in the core of well-designed conventional electrical machines.

Figure 1 shows the relative permeability μ_r and the specific losses P_{Fe} versus B of four different M400-50A samples from different manufacturers. The materials with the highest and lowest μ_r in the chosen range of B (see the gray box of Fig. 1a) are identified as M400a and M400b, respectively.

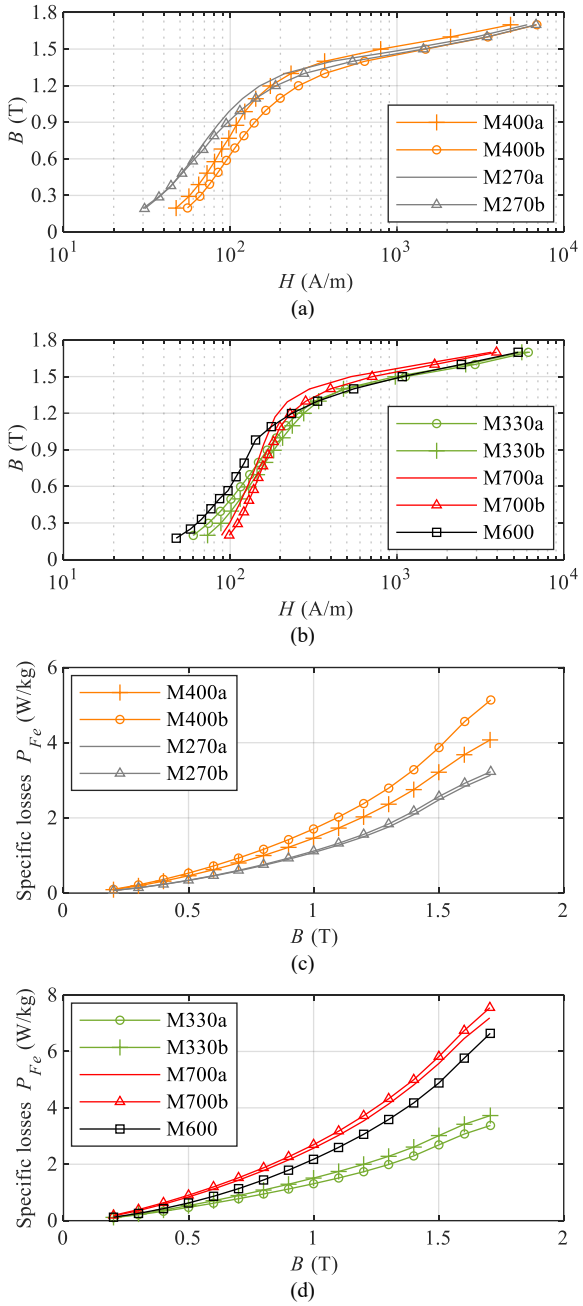

Fig. 2. The magnetic characteristics of the investigated materials. (a), (b) The *BH* (magnetization) curves; (c), (d) the specific power losses. The *BH* curves were characterized at low field levels and far from saturation. Proper extrapolation strategies must be therefore considered.

Figure 2 depicts the measured magnetic properties of all the chosen materials belonging to the different grades investigated in this study. The effect of their magnetic properties on the machine performance is carefully analyzed in Section IV. The nomenclature is the same used for the materials shown in Fig. 1. The *BH* curves illustrated in Fig. 2a and Fig. 2b highlight that the experimental characterizations were limited to low field levels. The measurements were indeed performed up to a magnetic field intensity H = 4-7 kA/m. To recognize how far from saturation the materials were characterized during the

experiments, it is possible to evaluate their p.u. differential permeability D (1).

$$D = \frac{1}{\mu_0} \cdot \frac{dB}{dH} \tag{1}$$

μ_0 is the permeability of vacuum, $4\pi \cdot 10^{-7}$ H/m. For all the materials represented in Fig. 2, the value for the differential permeability at the last data point n is in the range D_n = 23-35. Such values indicate that the materials were characterized too far from saturation. In case such material curves would be inputted in FEM software routines, errors in the numerical simulation may occur [10]. This can be avoided if a proper extrapolation of the BH curves to saturation is considered.

III. Methods to Extrapolate the Magnetization Curves

The commercial FEM software used in the study was Altair FLUX 2D, 2019 version. The software extends by default a user-defined BH curve using a linear extrapolation method, which considers the differential permeability of the last point D_n. This method assumes that above the measurement range, whatever the field level, the differential permeability (1) is a constant. When experiments are performed far from the magnetic saturation, such extrapolation completely ignores its physics, thus causing simulation errors.

The following provides a comparison between different extrapolation methods available in the literature. The aim is to find a suitable strategy for the purposes of the research presented in this paper.

A reference magnetization curve characterized up to saturation (D = 1) was chosen to validate the extrapolation results. The curve belongs to an M36 steel grade, it is available in the software FEMM, and it is pictured in Fig. 3. The curve was purposely truncated at suitable low and medium field values to evaluate two conditions: D_n = 34.6 and D_n = 8.9.

A. Linear Extrapolation method (LE)

This method for extrapolation is the one used by default by the FEM software Altair FLUX 2D, 2019 version. By naming the last two data points (n) and (n – 1), the value for D_n corresponds to the slope of a linear function (2).

$$D_n = \frac{1}{\mu_0} \cdot \frac{B_n - B_{n-1}}{H_n - H_{n-1}} \tag{2}$$

In (2), (n): (B_n, H_n) and (n – 1): (B_{n-1}, H_{n-1}). Any BH curve is extended to higher field levels using a linear function, slope D_n.

B. Law of Approch to Saturation method (LAS)

The LAS extrapolation relies on an experimental law widely treated in the scientific literature on magnetism. Its simplified form is reported in (3) [11].

$$M = M_S \cdot \left(1 - \frac{b}{H^2}\right) \tag{3}$$

M and M_S represent the magnetization and the saturation magnetization in A/m, respectively. The coefficient b can be calculated analytically.

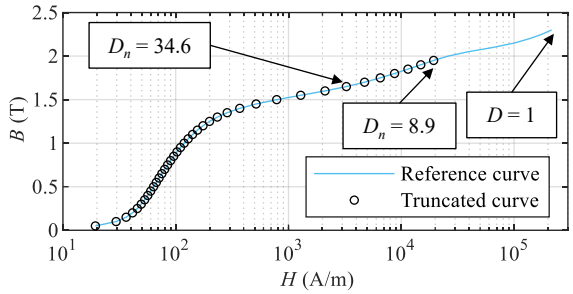

Fig. 3. The reference magnetization curve of an M36 steel used to validate the results of different extrapolation methods. The reference curve is truncated at suitable low (D_n = 34.6) and medium (D_n = 8.9) field levels to validate the extrapolation results in two different cases. D =1 indicates the saturation.

The magnetization M in (3) depends on two unknowns, M_S and b. This means that their value can be calculated by solving a system of two equations in two unknowns, i.e., (1) and (3). This analytical procedure imposes the continuity of D and B at the last data point n. Equation (3) must be expressed in terms of magnetic flux density $B = \mu_0 \cdot (H + M)$.

C. Simultaneous Exponential Extrapolation method (SEE)

The SEE methodology was presented in [10] and its expression can be written in terms of $B(H)$ as in (4).

$$B = J_S \cdot \left(1 - ue^{-vH}\right) + \mu_0 \cdot H \tag{4}$$

J_S is the saturation induction in T. The coefficients u, v can be calculated analytically solving simultaneously (1) and (4) by imposing the continuity of D and B at the last data point n. J_S can be estimated empirically from the resistivity ρ of the material in μΩ·cm (5) [10].

$$J_S = 2.2041 - 0.003726 \cdot \rho \tag{5}$$

The value for ρ of the reference M36 steel is provided in FEMM. The resistivity of the strips analyzed in this work was measured experimentally following the procedure suggested by the international standards [12].

D. Quadratic Extrapolation method (QE)

The quadratic extrapolation method QE was proposed in [13] and analyzed in [14]. The magnetic field intensity H is considered as a quadratic function of B for $D_n < D < 1$, and a linear function of B in saturated conditions, i.e., when D = 1 (6).

$$\begin{aligned} H &= a_2 \cdot B^2 + a_1 \cdot B + a_0, && D_n \le D < 1 \\ H &= (B - J_S)/\mu_0, && D = 1 \end{aligned} \tag{6}$$

J_S can be estimated using (5). The parameters a_0, a_1 and a_2 can be calculated using an analytical approach. It is necessary to impose the continuity of the function $1/D = \mu_0 \cdot dH/dB$ and of the functions $H(B)$ defined in (6). This must be done at both the last data point n and at the saturation point [14].

Figure 4 – Fig. 6 illustrate and compare the results of the presented extrapolation methodologies, including the relative extrapolation error ε, when considering D_n = 34.6 and D_n = 8.9.

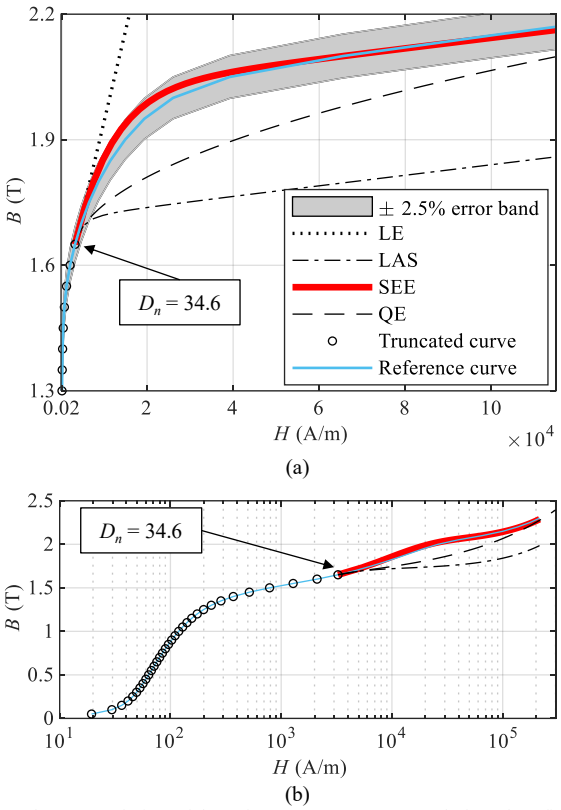

Fig. 4. The extrapolation of the reference curve (M36 steel) from low field levels ($D_n = 34.6$) to saturation using different strategies. (a) Detailed view and (b) full view. The SEE method provides the best extrapolation results.

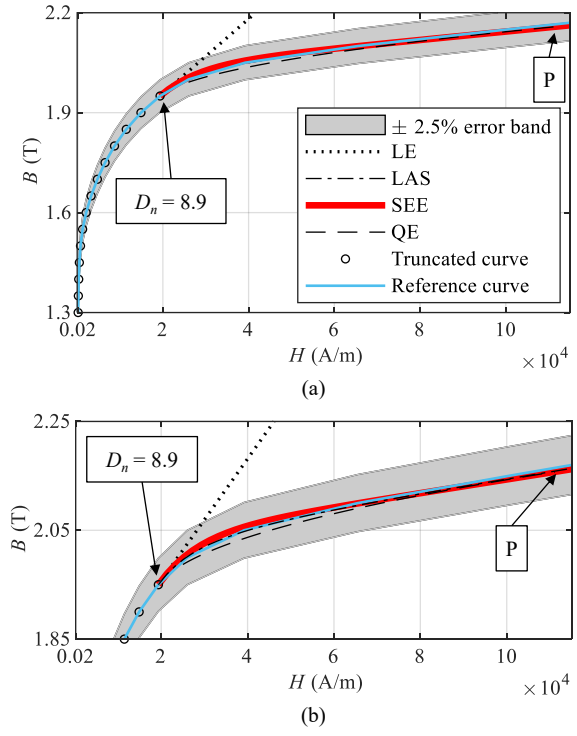

Fig. 5. The extrapolation of the reference curve (M36 steel) from medium field levels ($D_n = 8.9$) to saturation using different strategies. (a) Detailed view and (b) zoom-in. The LAS and SEE methods are the most accurate ones. The QE method misestimates the value of the field in saturated conditions (point P).

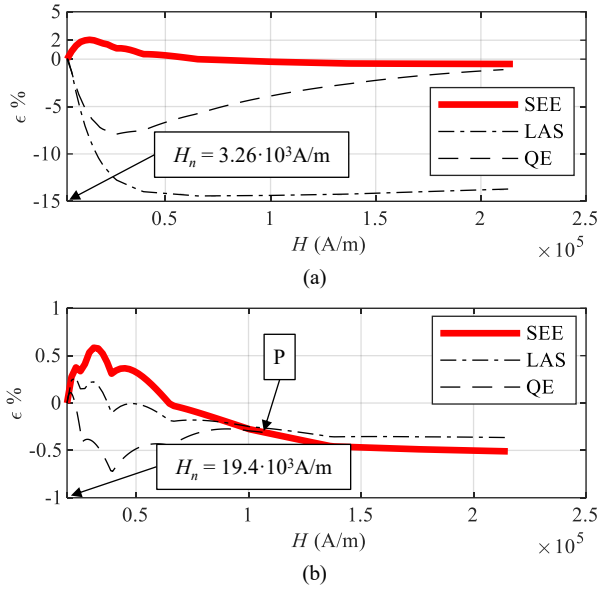

Fig. 6. The relative extrapolation error of the discussed methods. (a) Error in extrapolating the reference curve from the low fields ($H_n = 3.26$ kA/m, $D_n = 34.6$) and (b) error in extrapolating the reference curve from the medium field levels ($H_n = 19.4$ kA/m, $D_n = 8.9$).

The extrapolated values for B, in both the LAS and SEE approaches, were calculated up to $H = 2.15 \cdot 10^5$ A/m; such value comes from the saturation point of the reference curve (Fig. 3). For the QE method, the values for B and H were calculated analytically by solving (6). A preliminary check was carried out to validate the accuracy of (5). The value for J_S of the reference curve is 2.0295 T, and the predicted value with (5) is 2.0178 T. An error lower than 1% was considered totally acceptable.

Figure 4 depicts the extrapolation results when the data are available at low field levels. The last point features $B_n = 1.65$ T, $H_n = 3.26$ kA/m and $D_n = 34.6$. The results show that the QE and the LAS approaches fail to correctly extrapolate the reference curve to saturation. The QE method also overestimates the saturation point at field levels ~$3 \cdot 10^5$ A/m, as it can be seen in Fig. 4b. The SEE method provides the most accurate results, exhibiting an extrapolation error lower than 2.5% over the whole field range. Special attention must be paid to the linear extrapolation approach (LE), which ignores the physics of saturation, and provides, in this case, unrealistic results. The extrapolation results from the data at medium field levels are illustrated in Fig. 5. The last data point now features $B_n = 1.95$ T, $H_n = 19.4$ kA/m and $D_n = 8.9$. The LE method still provides unrealistic results, while all the others, LAS, SEE and QE, provide accurate results in extrapolating the reference curve to saturation. The LAS extrapolation, which physically describes the saturation of soft magnetic materials, and the SEE method can be considered equivalent in this case (Fig. 5b). Despite its good accuracy, the QE method misestimates the saturation point: the material is considered to saturate at point P in Fig. 5, which is well below the actual saturation of the reference curve. Figure 6 compares the relative extrapolation error ε of the discussed methods in the two cases, $D_n = 34.6$ and $D_n = 8.9$. Such error is computed as in (7).

$$\varepsilon_{\%} = \left(B_{extr} / B_{ref} - 1\right) \cdot 100 \tag{7}$$

B_{extr} refers to the values of B computed by the extrapolation methods, while B_{ref} are taken from the reference curve. The comparison was carried out at imposed field intensity levels.

The analysis of Fig. 6 allows to draw some conclusion about the extrapolation of *BH* curves. When only measured data at low field levels, i.e., $H \sim 3$ kA/m in this case, are available (much common in practice), the SEE method can be successfully used with a very low error to extrapolate the *BH* curves to saturation. Instead, when data up to medium field levels, i.e., $H \sim 20$ kA/m in this case, are available, both the LAS and SEE can provide good extrapolation results, keeping in mind that LAS physically describes the physics of saturation in soft magnetic materials. QE can be also used in this case, but a misestimation of the saturation point (label P in both Fig. 5 and Fig. 6b), at least in this case, may be expected.

The experimental *BH* curves in Fig. 2 belonging to the investigated materials were extrapolated to saturation using the SEE approach. In this way, they were ready to be inputted in the FEM software used in this study.

IV. Impact of the Core Material on Machine Performance

After extrapolating the measured *BH* curves to saturation, it was possible to run FEM simulations to evaluate the machine performance. In this Section, the reference machine is discussed first. The impact of different rotor and stator steel grades on the performance of the machine is discussed afterwards, comparing the variation of the air gap power and the core losses.

A. The reference WFSM investigated in the study

The geometry of the reference WFSM is pictured in Fig. 7. It features a three-phase distributed winding on the stator and field windings mounted on the salient-pole rotor (Fig. 7a). To simplify the analyses, damper windings on the rotor were not included in the study. The stator core, the pole shoe and the pole neck were modeled as laminated regions, and the material is M400b, see Fig. 2. The rotor yoke was modeled as solid steel with an assigned *BH* curve that was not modified throughout the whole study. In the simulations, the electrical conductivity of all the magnetic parts was set to zero, thus disregarding the reaction field due to the eddy currents in the core. The shaft was assumed to be nonmagnetic. The FEM model was solved by running 2D time-dependent studies, and the machine was supplied injecting current in both the stator and the rotor windings. No external circuit was coupled to the FEM domain, thus disregarding the end effects. The main specifications of the machine are listed in Table I; it operates in the generating mode, at the rated power, and in overexcited conditions, as highlighted by the power factor $cos\varphi$. The mesh of the domain is illustrated in Fig. 7b: it was carefully refined in the proximity of the air gap to accurately compute the electromagnetic torque. The flux diagram of the loaded machine in Fig. 7c clearly shows the distortion of the field due to the armature reaction. The magnetic flux density plot in Fig. 7d shows how the generator is magnetically loaded. The local saturation occurring at the point Q is the main responsible for the torque ripple of the machine [7]. At point Q, B reaches a reasonable value of 2.56 T.

During preliminary simulations it was verified that the use of a linear extrapolation for the *BH* curve of the material M400b led to an unrealistic value of B of ~4.7 T at point Q.

TABLE I. Main Specifications of the Reference Machine.

Parameter	*Value*
Rated power P_{out}	1.16 MW
Number of phases	3
Number of pole pairs	2
Number of stator slots	84
Rated frequency	50 Hz
Rated stator current I_S	902 A
Rated field current density J_f	6 A/mm^2
Power factor $cos\varphi$	0.8 leading

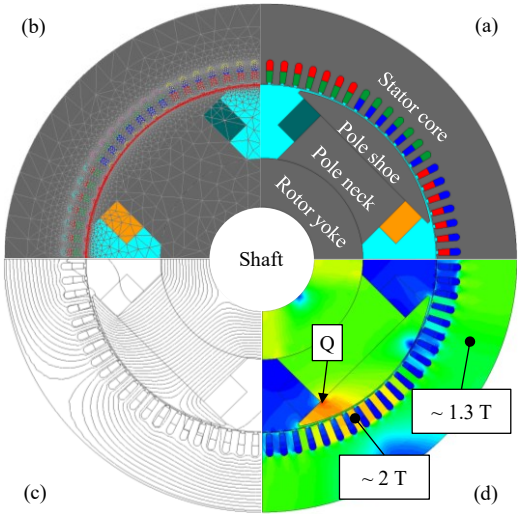

Fig. 7. The reference WFSM investigated in the study. From the top right in counterclockwise direction: (a) the geometry of the machine; (b) the finite-element mesh of the domain, highlighting the fine mesh of the air gap regions; (c) the flux diagram at load (vector potential isolines), and (d) the plot of the magnetic flux density distribution at load. The label Q indicates the point at which the maximum value of B occurs (2.56 T).

The fundamental air gap flux density (normal component) was overestimated by ~13% at no-load and by ~8% at load, respectively. The electromagnetic torque at the rated load was overestimated by ~18%. It is logical to expect an overestimation of the core losses as well. These results revealed once again the importance of a proper extrapolation of the measured *BH* curves to saturation to avoid simulation errors.

The core losses were calculated at the postprocessing stage using the model (8), which is implemented in the FEM software used for the investigations [15].

$$P_{Fe} = k_{hyst} \cdot f_m \cdot B_p{}^2 + \frac{\sigma d^2}{12T} \cdot \int_0^T \left(\frac{dB}{dt} \right)^2 dt + \frac{k_{exc}}{T} \cdot \int_0^T \left| \frac{dB}{dt} \right|^{3/2} dt \quad (8)$$

This three-term model separates the measured power losses in soft magnetic materials in the hysteresis, classical and excess loss components. P_{Fe} represents the total specific losses of the steels in W/kg, f_m is the supply frequency, $T = 1/f_m$ is the electrical period of the supply currents, B_p is the peak value of the magnetic flux density, σ represents the conductivity of the sheets, and d stands for their thickness. The classical and excess losses are determined starting from the time derivative of B in the core over one electrical period, while the hysteresis losses depend on the peak value of B. The coefficients k_{hyst} and k_{exc} were determined to fit the experimental power loss versus B curves shown in Fig. 2, Section II.

B. *Influence of the rotor and the stator lamination material on the machine performance*

The influence of different rotor lamination materials on the machine performance was investigated first. Table II reports which parts of the rotor core were modeled using the materials presented in Section II. The name of the various investigated machine models is the same used for the material employed on the rotor.

The evaluation of the performance was carried out considering the change in the air gap power. The machine models were compared at the same supply conditions, meaning that the stator current and the rotor current density of the reference machine reported in Table I were imposed to all the machine models. This allowed to disregard the impact of the Joule losses. The mechanical losses were considered unchanged.

Before comparing to each other the machines with different rotor lamination materials, it was necessary to assess the impact of the core losses on the air gap power. If the core losses represent a small portion of the airgap power, it is possible to directly compare the machines observing the change in the air gap power itself. It was verified that the core losses account for less than 1% of the air gap power for all the machines, and this allowed to validate the preliminary assumption discussed above.

Figure 8 compares the p.u. core losses and the p.u. air gap power of the analyzed machines with different rotor lamination materials. The illustrated quantities are displayed here in p.u. for convenience. For clarity, the considered air gap power of the reference machine was the rated one (1.16 MW) and the value for its core losses is about 6.2 kW. Those losses were calculated in the laminated regions of the core, i.e., the stator core, the rotor pole shoe and the rotor pole neck. The simulations showed that most of the core losses occur in the stator and a minor part on the surface of the pole shoe. The latter are mainly eddy-current losses due to the spatial harmonics and the slotting effect. The variation of the core losses in Fig. 8a can be considered reasonable, despite the operation of the machines at a slightly different flux per pole, and consequently a slightly different air gap power, as shown in Fig. 8b. A different rotor lamination material causes a slight change in the core losses. The greatest increment is about 14% and occurs when using the material M600. This result is not unexpected since the M600 steels are 0.65 mm thick, and therefore they may exhibit larger eddy-current losses. The opposite applies for the M330 steels that are 0.35 mm thick, thus exhibiting lower eddy-current losses; in this case the decrement of the core losses is about 5%.
The analysis of Fig. 8b shows that the use of the M330a steel on the rotor led to a 1.1% decrement of the air gap power, while the use of the M700a steel resulted in a 1.6% increment.

To recognize the actual difference in terms of performance of the machines with different steel sheets, it was necessary to compare them to the reference at the same air gap power. It was decided to restrict the further analyses presented in this paper on the machine M700a, which was the one providing the highest increase in the air gap power, as seen in Fig. 8b. In particular, it was decided to investigate a machine with an M700a steel on both the stator and the rotor, identified as M700S in Table II.

Figure 9 provides the comparison among the reference machine and the machines M700a and M700S, showing the change in both the air gap power and the core losses. The use of the M700a steel sheets on both the rotor and the stator resulted in a 3.8% increase in the air gap power. Such improvement was considered quite relevant, also giving the fact that the machines were compared at the same supply conditions. The expected increase in the core losses was remarkable, about 73%.
The comparisons shown in Figs. 8-9 do not provide a full picture of the differences between the machines REF and M700S. Therefore, another strategy is used in the next Section, allowing for a comparison at constant air gap power.

TABLE II. MATERIALS FOR THE IRON CORE TO ASSESS THE IMPACT OF DIFFERENT ROTOR AND STATOR LAMINATIONS ON MACHINE PERFORMANCE.

Machine model	**Core material**		
	Stator core	***Rotor pole***	***Rotor yoke***
REF (reference)	M400b	M400b	Solid steel with an assigned *BH* curve
M270a		M270a	
M270b		M270b	
M330a		M330a	
M330b		M330b	
M400a		M400a	
M700a		M700a	
M700b		M700b	
M600		M600	
M700S	**M700a**		

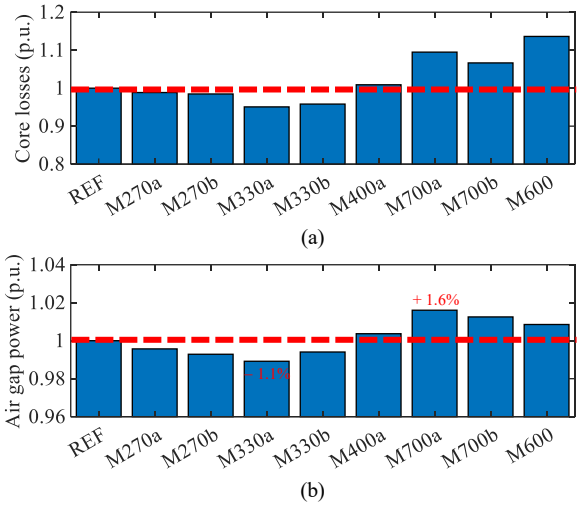

Fig. 8. The influence of different rotor lamination materials on the machine performance. (a) p.u. core losses and (b) p.u. air gap power. The red dashed lines were plotted to indicate the 1 p.u. The machines were supplied with the same stator current and rotor current density. The highest improvement in the air gap power was 1.6% and this was obtained for the machine M700a.

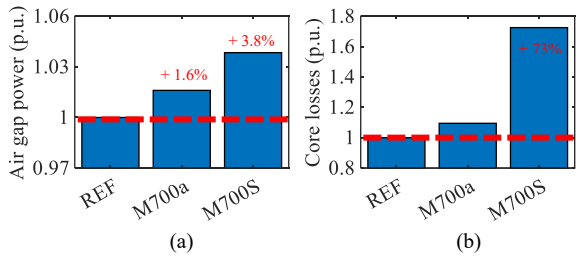

Fig. 9. The impact of a different grade of the rotor and the stator steel sheets on the machine performance. (a) p.u. air gap power and (b) p.u. core losses. The red dashed lines were plotted to indicate the 1 p.u. The use of the M700a material in the whole core allowed to obtain a 3.8% increase in the air gap power. The core losses increased by 73%, but at different air gap power, i.e., air gap flux.

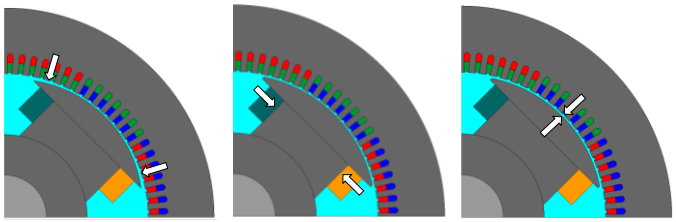

(a) (b) (c)

Fig. 10. The proposed geometrical modifications of the rotor pole geometry. (a) Change in the curvature radius of the pole surface; (b) adjustment of the width of the pole neck and (c) modification of the air gap size under the *d* axis. Such modifications of the rotor geometry allowed to compare the machines REF and M700S at the same air gap power.

V. Influence of the Rotor Pole Geometry on Machine Performance

The most relevant comparison approach of the machine models REF and M700S requires to evaluate their performance at the same supply conditions as well as at the same air gap power. The chosen strategy involved different modifications of the rotor pole geometry of the machine M700S with the aim to reach the reference air gap power. Three different geometrical strategies were selected, as shown in Fig. 10.

A. Strategy 1: pole arc radius

The first geometrical strategy is illustrated in Fig. 10a, and it involved a modification of the pole arc surface. Here, the air gap size under the *d* axis was kept unchanged, while the air gap size towards the *q* axis was enhanced with respect to the reference rotor pole geometry. The white arrows in Fig. 10a help understanding the proposed geometrical modification. Such method can be considered as an alternative to the well-known inverse-cosine approach for the design of the air gap of WFSMs. A similar strategy was also proposed in [16], for permanent magnet machines. Using such strategy, improvements in the torque ripple were expected.

B. Strategy 2: rotor neck width

The second geometrical strategy proposed a modification of the pole neck width, as depicted in Fig. 10b, and highlighted using the white arrows. Such strategy can help to reduce the flux per pole and therefore to bring the air gap power to the reference level. Mechanical advantages were expected from this strategy since it can help to reduce the mass of the rotor iron.

C. Strategy 3: d-axis air gap size

The last considered strategy was to alter the height of the rotor neck, i.e., an increase of the air gap size under the *d* axis. It is illustrated in Fig. 10c, with the help of the white arrows. Benefits in terms of torque ripple reduction were expected using this strategy.

A sensitivity analysis was carried out considering all the three geometrical strategies, and to find out for which variations of the rotor dimensions it was possible to reach the reference air gap power. The results revealed that the use of strategy 1 alone did not allow to reach the reference air gap power. The permitted modifications of the curvature of the rotor pole surface were limited because of practical reasons related to both the manufacturing and the assembly processes of the machine. A maximum 7% reduction of the curvature radius was imposed.

TABLE III. The Effect of the Rotor Geometry Modification on Machine Performance using Strategy 1 and Strategy 2.

Performance parameter	Machine model	
	REF	**M700S**
Torque ripple ΔT %	7.94%	3.12%
Core losses P_{core} (kW)	6.2	8.8
Rotor core mass m_{rot} (kg)	112.5	108.2

TABLE IV. The Effect of the Rotor Geometry Modification on Machine Performance using Strategy 2.

Performance parameter	Machine model	
	REF	**M700S**
Torque ripple ΔT %	7.94%	8.03%
Core losses P_{core} (kW)	6.2	10.2
Rotor core mass m_{rot} (kg)	112.5	107.9

TABLE V. The Effect of the Rotor Geometry Modification on Machine Performance using Strategy 3.

Performance parameter	Machine model	
	REF	**M700S**
Torque ripple ΔT %	7.94%	6.77%
Core losses P_{core} (kW)	6.2	9.3
Rotor core mass m_{rot} (kg)	112.5	113

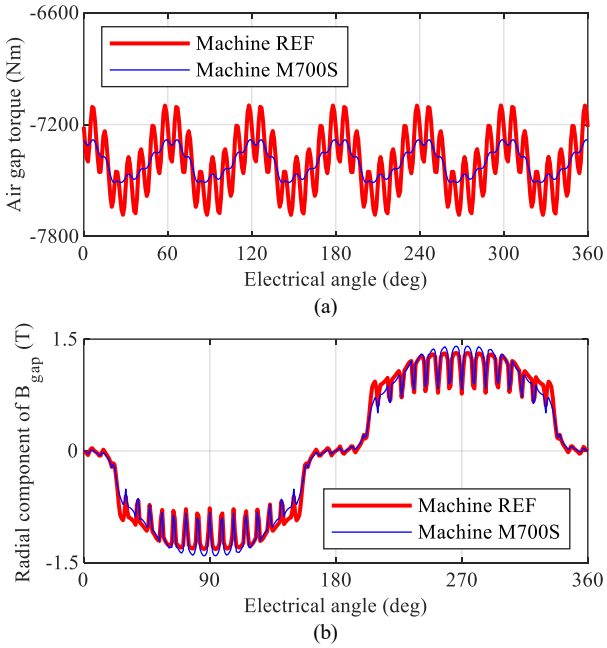

Fig. 11. The effect of combining strategy 1 and strategy 2 on the performance of the machine M700S. (a) Comparison between the air gap torque of the reference machine (REF) and of the machine M700S. (b) Comparison between the radial component of the air gap flux density of the reference machine (REF) and of the machine M700S. The reduction of the torque ripple can be attributed to a more sinusoidally-shaped air gap flux density.

Strategy 1 was therefore investigated together with strategy 2.

Table III – Table V and Fig. 11 report the results of the geometrical modifications applied to the rotor pole geometry of machine M700S. The machines REF and M700S are now compared at the same air gap power, and this allowed for a fair evaluation of the influence of both the lamination material and the rotor pole geometry on the machine performance.

Table III presents the results combining strategy 1 and 2.

The pole arc radius was reduced by its maximum allowed value, that is, 7%, while the rotor neck width was reduced by 5%. This combination allowed to reach the reference air gap power. The torque ripple was more than halved, passing from 7.94% for the reference machine to 3.12% for the M700S machine with a modified rotor pole geometry. This can be observed in Fig. 11, where both the air gap torque (Fig. 11a) and the air gap flux density (Fig. 11b) of machine REF and M700S are compared. The use of strategy 1 mainly contributed to such improvement. An almost 42% increase of the core losses for the M700S machine with regard to the REF machine was expected because of the use of a higher-grade steel for the rotor and stator laminations. A 4% decrease of the mass of the rotor iron can be beneficial from the mechanical point of view.

Table IV reports the results of using strategy 2, reducing the rotor neck width by 7.3%. The main advantage is an almost 4% reduction of the mass of the rotor iron. The torque ripple slightly increased compared to the reference machine, and a further increase of the core losses was observed with respect to the results reported in Table III.

Table V summarizes the results in applying strategy 3, with which the *d*-axis air gap size was increased by 34%. The larger air gap size slightly reduced the impact of the higher order spatial harmonics in the air gap due to the slotting effect and the winding distribution. This resulted in a slight decrease of the torque ripple. The core losses are in between those obtained with strategy 2 and those combining strategy 1 and 2. The mass of the rotor iron was basically the same, with an almost imperceptible variation due to the higher mass density of the M700 steels compared to the M400 (reference machine).

Based on the obtained results, it can be concluded that, at least for the present investigations, the best compromise can be achieved using strategy 1 and 2 together (Table III).

VI. Conclusion

The present paper investigated the influence of the core material and of the rotor pole geometry on the steady-state performance of a wound field synchronous generator. The results are based on FEM analyses.

The studies on the laminated materials concentrated on NO SiFe steel sheets of various grades, and from different suppliers. Their experimental characterizations at low field levels revealed the need for a proper extrapolation method of their *BH* curves to saturation. Among different strategies, the SEE method was selected, since it provided an extrapolation error lower than 2.5% over the whole field range.

The impact of various rotor lamination materials on machine performance was assessed first. The use of a high-grade steel provided the highest improvement in the air gap power, and a further enhancement was obtained using the same steel sheets also on the stator side. The comparisons were carried out with respect to the reference machine in the same supply conditions.

To assess the actual performance improvement, different machines must be compared at the same air gap power. To do so, the rotor pole geometry was modified using different geometrical strategies with the aim to reach the reference air gap power. The results showed that a combined modification of the pole arc radius and of the rotor neck provided the best results. Compared to the reference machine, the new machine featured a significantly reduced torque ripple and a slightly reduced mass of the rotor iron. An increase in the core losses was observed, mainly because of using the high-grade steel sheets for the core.

Future research activities may include the investigation of different combinations of materials for the stator and the rotor laminations. Additional modifications of the rotor geometry can be also assessed, i.e., the use of asymmetric configurations for the pole shoe. Lastly, the studies should take into consideration the influence of the manufacturing process on the magnetic properties of the laminations.

References

[1] F. Graffeo, S. Vaschetto, M. Cossale, M. Kerschbaumer, E. C. Bortoni, and A. Cavagnino, "Cylindrical Wound-Rotor Synchronous Machines for Traction Applications," in *2020 International Conference on Electrical Machines (ICEM)*, 2020, vol. 1, pp. 1736–1742.

[2] A. Di Gioia *et al.*, "Design and Demonstration of a Wound Field Synchronous Machine for Electric Vehicle Traction With Brushless Capacitive Field Excitation," *IEEE Trans. Ind. Appl.*, vol. 54, no. 2, pp. 1390–1403, 2018.

[3] K. Yamazaki, K. Tanaka, and M. Ohto, "Impact of Core Material Grades on the Performance of Variable Speed Induction Motors Fed by Inverters," *IEEE Trans. Ind. Appl.*, vol. 54, no. 6, pp. 5833–5842, 2018.

[4] D. Kowal, L. Dupré, P. Sergeant, L. Vandenbossche, and M. De Wulf, "Influence of the electrical steel grade on the performance of the direct-drive and single stage gearbox permanent-magnet machine for wind energy generation, based on an analytical model," *IEEE Trans. Magn.*, vol. 47, no. 12, pp. 4781–4790, 2011.

[5] C.-T. Liu, H.-Y. Chung, and S.-Y. Lin, "On the electromagnetic steel selections and performance impact assessments of synchronous reluctance motors," *IEEE Trans. Ind. Appl.*, vol. 53, no. 3, pp. 2569–2577, 2017.

[6] A. Frias *et al.*, "Rotor and stator shape optimization of a synchronous machine to reduce iron losses and acoustic noise," in 2012 IEEE Vehicle Power and Propulsion Conference, 2012, pp. 98–103.

[7] S.-H. Do, B.-H. Lee, H.-Y. Lee, and J.-P. Hong, "Torque ripple reduction of wound rotor synchronous motor using rotor slits," in 2012 15th International Conference on Electrical Machines and Systems (ICEMS), 2012, pp. 1–4.

[8] W. Liu and T. A. Lipo, "On saliency enhancement of salient pole wound field synchronous machines," in 2016 IEEE Energy Conversion Congress and Exposition (ECCE), 2016, pp. 1–8.

[9] "Methods of measurement of the magnetic properties of electrical steel strip and sheet by means of an Epstein frame." International Standard IEC 60404-2:2008.

[10] D. K. Rao and V. Kuptsov, "Effective use of magnetization data in the design of electric machines with overfluxed regions," *IEEE Trans. Magn.*, vol. 51, no. 7, pp. 1–9, 2015.

[11] A. E. Umenei, Y. Melikhov, and D. C. Jiles, "Models for extrapolation of magnetization data on magnetic cores to high fields," *IEEE Trans. Magn.*, vol. 47, no. 12, pp. 4707–4711, 2011.

[12] "Methods of measurement of resistivity, density and stacking factor of electrical steel strip and sheet." International Standard IEC 60404-13:2018.

[13] K. Fujiwara, T. Adachi, and N. Takahashi, "A proposal of finite-element analysis considering two-dimensional magnetic properties," *IEEE Trans. Magn.*, vol. 38, no. 2, pp. 889–892, 2002.

[14] S.-H. Chai, J.-H. Kim, S.-I. Kim, and J.-P. Hong, "Extrapolating BH Curve Data using Common Electrical Steel Characteristics for High Magnetic Saturation Applications," *J. Magn.*, vol. 20, no. 3, pp. 258–264, 2015.

[15] F. Fiorillo and A. Novikov, "An improved approach to power losses in magnetic laminations under nonsinusoidal induction waveform," *IEEE Trans. Magn.*, vol. 26, no. 5, pp. 2904–2910, 1990.

[16] S. A. Evans, "Salient pole shoe shapes of interior permanent magnet synchronous machines," in The XIX International Conference on Electrical Machines-ICEM 2010, 2010, pp. 1–6.